High-Throughput Techniques for Measuring the Spin Hall Effect

Markus Meinert,[1,*] Björn Gliniors,[2] Oliver Gueckstock,[3,4] Tom S. Seifert,[3,4] Lukas Liensberger,[5,6] Mathias Weiler,[5,6,7] Sebastian Wimmer,[8] Hubert Ebert,[8] and Tobias Kampfrath[3,4]

[1] *Department of Electrical Engineering and Information Technology, Technical University of Darmstadt, Merckstraße 25, 64283 Darmstadt, Germany*

[2] *Center for Spinelectronic Materials and Devices, Department of Physics, Bielefeld University, 33501 Bielefeld, Germany*

[3] *Department of Physics, Freie Universität Berlin, 14195 Berlin, Germany*

[4] *Fritz Haber Institute of the Max Planck Society, 14195 Berlin, Germany*

[5] *Walther-Meißner-Institut, Bayerische Akademie der Wissenschaften, 85748 Garching, Germany*

[6] *Physik-Department, Technische Universität München, 85748 Garching, Germany*

[7] *Fachbereich Physik and Landesforschungszentrum OPTIMAS, Technische Universität Kaiserslautern, 67663 Kaiserslautern, Germany*

[8] *Department Chemie, Ludwig-Maximilians-Universität München, 81377 Munich, Germany*

(Received 8 October 2020; accepted 11 November 2020; published 3 December 2020)

The spin Hall effect in heavy-metal thin films is routinely used to convert charge currents into transverse spin currents and can be used to exert torque on adjacent ferromagnets. Conversely, the inverse spin Hall effect is frequently used to detect spin currents by charge currents in spintronic devices up to the terahertz frequency range. Numerous techniques to measure the spin Hall effect or its inverse have been introduced, most of which require extensive sample preparation by multistep lithography. To enable rapid screening of materials in terms of charge-to-spin conversion, suitable high-throughput methods for measuring the spin Hall angle are required. Here we compare two lithography-free techniques, terahertz emission spectroscopy and broadband ferromagnetic resonance, with standard harmonic Hall measurements and theoretical predictions using the binary-alloy series Au_xPt_{1-x} as a benchmark system. Despite their being highly complementary, we find that all three techniques yield a spin Hall angle with approximately the same x dependence, which is also consistent with first-principles calculations. Quantitative discrepancies are discussed in terms of magnetization orientation and interfacial spin-memory loss.

DOI: 10.1103/PhysRevApplied.14.064011

I. INTRODUCTION

The spin Hall effect [1–4] (SHE) converts a charge current with density j_c into a transverse spin current with density j_s. The charge-to-spin conversion efficiency can be characterized by the spin Hall angle (SHA) $\theta_{SH} = j_s/j_c$. It is commonly written as $\theta_{SH} = \sigma_{SH}/\sigma_{xx}$, where σ_{SH} is the spin Hall conductivity (SHC) and σ_{xx} is the longitudinal conductivity along the direction of the charge-current flow. Both intrinsic effects that are already present in perfectly periodic crystals and extrinsic effects, (i.e., skew scattering and side-jump scattering) contribute to the spin Hall angle. In most practical cases, the electron scattering rate in a material is large due to point defects, grain boundaries, and phonons; therefore, the intrinsic mechanism dominates σ_{SH}. Following theoretical predictions [5], various crystalline heavy metals (HMs) with large spin Hall conductivity were experimentally confirmed, such as Pt [6], β-W [7], and β-Ta [8].

The SHC of crystalline materials is experimentally [6,9–12] and theoretically [5,13–16] well understood. The relation $\theta_{SH} = \sigma_{SH}/\sigma_{xx}$ was experimentally studied for Pt thin films [6]. This study partially explains the large range of reported SHAs in the literature for a single material and rationalizes the somewhat counterintuitive observation that thin films of lower quality and thus lower conductivity σ_{xx} have a larger SHA [4]. By alloying Pt with Au, it was shown that σ_{xx} can be decreased to increase the SHA [17].

The spin current originating from the SHE can be injected into an adjacent ferromagnetic (FM) layer, where it gives rise to so-called fieldlike and dampinglike spin-orbit torques (SOTs) [18,19]. These may induce precession of the magnetization [20], domain-wall motion [21], and

*markus.meinert@tu-darmstadt.de

switching of the magnetization orientation [7,8,22]. Various promising concepts for SHE-based magnetic memory devices, so-called SOT magnetic random-access memories were proposed [23–26].

To quantify the SHA or the SHC experimentally, numerous techniques were developed, as detailed in Refs. [3,4]. The various techniques can differ significantly, for example, with respect to the driving perturbation, probed observable magnetization, and external-field geometry, use of either the direct SHE or the inverse SHE, and the frequency range covered. On one hand, several ferromagnetic resonance- (FMR) based techniques were used, such as (i) FMR spin pumping with subsequent detection of the inverse SHE [27] and (ii) SHE-induced modulation of the linewidth in a FMR experiment due to the action of the dampinglike torque from the spin current [28]. The quantification of the SHE relies on either measuring the rectified voltages generated by the inverse SHE or determining the modulation of the FMR linewidth, which originates from the dampinglike spin-orbit torque. On the other hand, electrical transport techniques were developed that use nonlocal spin injection [29], the spin Hall magnetoresistance [30],and magnetic loop shifts [31] or measure the deflection of the magnetization and the resulting change in the anomalous Hall effect [8]. All of these techniques are, in principle, quantitative and have in common that relatively tedious lithographic preparation of microdevices is required.

Materials with a large SHA can be tailored by alloying [17,32,33], which decreases the conductivity and tunes the Fermi level close to maxima of the SHC. Also, phase transitions in binary or ternary phase diagrams can be used, or amorphous metals with low conductivity may be created by enforced mixing of immiscible elements [34]. The associated maxima in the SHA as a function of composition can be quite narrow, such that optimization requires a large number of samples to be investigated. Lithography is time-consuming and thus a limiting factor for high-throughput SHA characterization. Therefore, compatible methods that do not require any additional processing steps are highly desirable. Recently, two promising techniques potentially fulfilling this need have become available: terahertz emission spectroscopy [TES; Figs. 1(a) and 1(d)] and vector-network-analyzer (VNA) FMR [Figs. 1(b) and 1(e)]. Despite their relevance for rapid sample characterization, their performances have

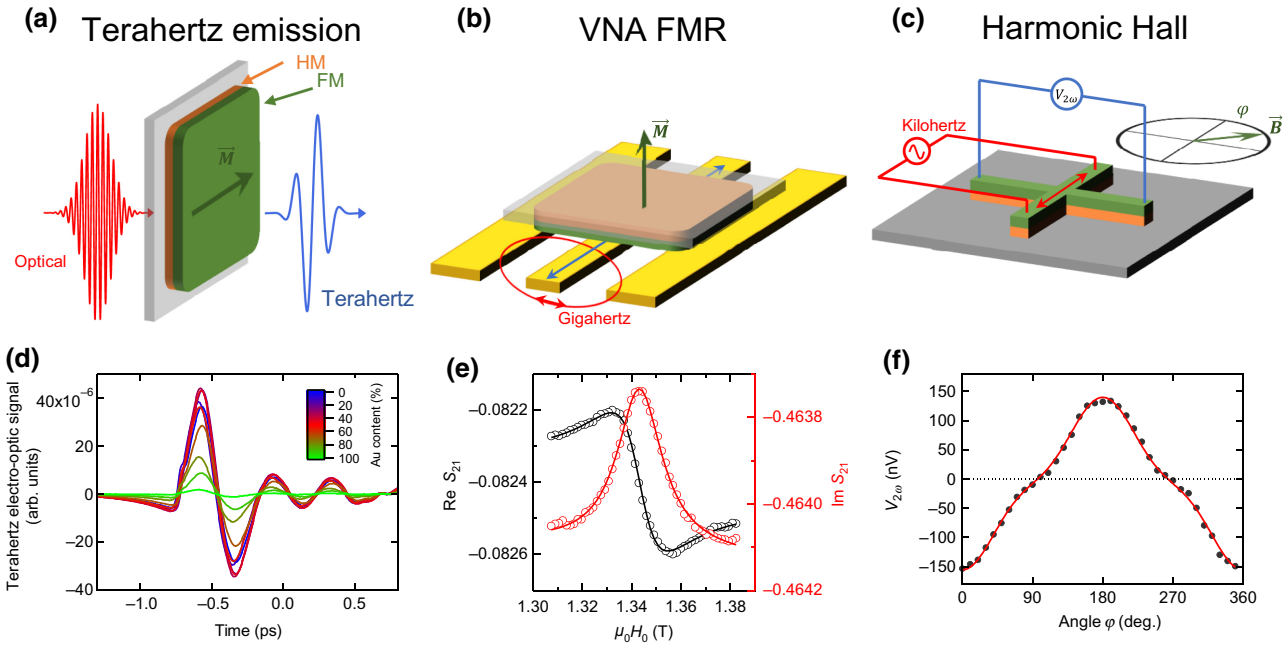

FIG. 1. Overview of three different techniques to determine the spin Hall angle of a material as described in the main text. The top row shows schematics of the techniques (not to scale), while the bottom row shows typical raw data. (a),(d) Terahertz emission spectroscopy: an optical laser pulse generates an ultrafast heat pulse in the films. Because of the spin-dependent Seebeck effect, a spin current flows from the FM layer into the HM layer. The inverse spin Hall effect converts the spin current into a charge pulse, which emits terahertz radiation. (b),(e) VNA FMR: a gigahertz current in the coplanar waveguide excites the ferromagnetic resonance in the FM layer. Spin pumping drives a spin current into the HM layer, where it is converted into an oscillating charge current. Its magnetic field couples into the waveguide and can be detected in the complex-valued waveguide transmission signal S_{21}. (c),(f) Harmonic Hall measurements: a kilohertz charge current drives an oscillating spin current from the HM layer into the FM layer. The associated spin-orbit torque drives an oscillating deflection of the magnetization out of the film plane. The associated oscillating anomalous Hall voltage is detected as a second-harmonic transverse voltage in the Hall cross.

not been compared with each other or with the performance of a well-established technique such as harmonic Hall response [HHR; Figs. 1(c) and 1(f)]. Recent work that experimentally compared the spin Seebeck effect at dc and terahertz frequencies indicates that TES has great potential for material characterization, with results that are consistent with those obtained by static methods [35].

Here we demonstrate that both TES and VNA FMR are suitable techniques to quickly obtain quantitative measurements of the SHA of a metallic binary-alloy series. Both methods do not require any postdeposition sample processing and feature data-acquisition times on the timescale of minutes (TES) to hours (VNA FMR). We compare the results from these two high-throughput methods with harmonic-Hall-response measurements, which use a single lithography step and serve as a reference [36–39]. In addition, we compare our results with first-principles calculations [17]. Although the three methods are very different in terms of frequency windows, spin-current generation, and detection schemes, we find qualitatively good agreement between them.

II. EXPERIMENTAL DETAILS

A. Sample system

To benchmark our techniques, we use a series of Au-Pt binary alloys. Thin-film stacks of Au_xPt_{1-x}(3 nm)/$Co_{40}Fe_{40}B_{20}$ (3 nm)/Si(1.5 nm) are grown by dc unbalanced magnetron co-sputtering in a 2-in. sputtering system at room temperature. For TES and VNA-FMR experiments, the samples are not processed any further. For the harmonic Hall measurements, the samples are patterned with Hall cross devices with fourfold rotational symmetry and a linewidth of 16 μm by standard optical lithography and Ar-ion-beam milling. All samples are checked by x-ray-diffraction, x-ray-reflectivity, x-ray-fluorescence, and four-point-dc-conductivity measurements.

The in-plane conductivities σ_{xx} of the Au-Pt alloy layers are shown in Fig. 2(a), where a parallel-conductor model is applied to remove the contributions from the $Co_{40}Fe_{40}B_{20}$ layers ($\sigma_{Co_{40}Fe_{40}B_{20}} = 5.7 \times 10^5$ S/m). The corresponding conductivity of the Pt layer (2.78×10^6 S/m) is quite typical for a thickness of 3 nm [6,10,40]. As expected, doping with Au reduces σ_{xx} substantially. The conductivity of Au-rich samples remains low, because of the pronounced island growth of Au on SiO_2 surfaces. In the following, we discuss key aspects of the spin Hall measurement techniques used and present respective results. Additional technical details are provided in the Appendix.

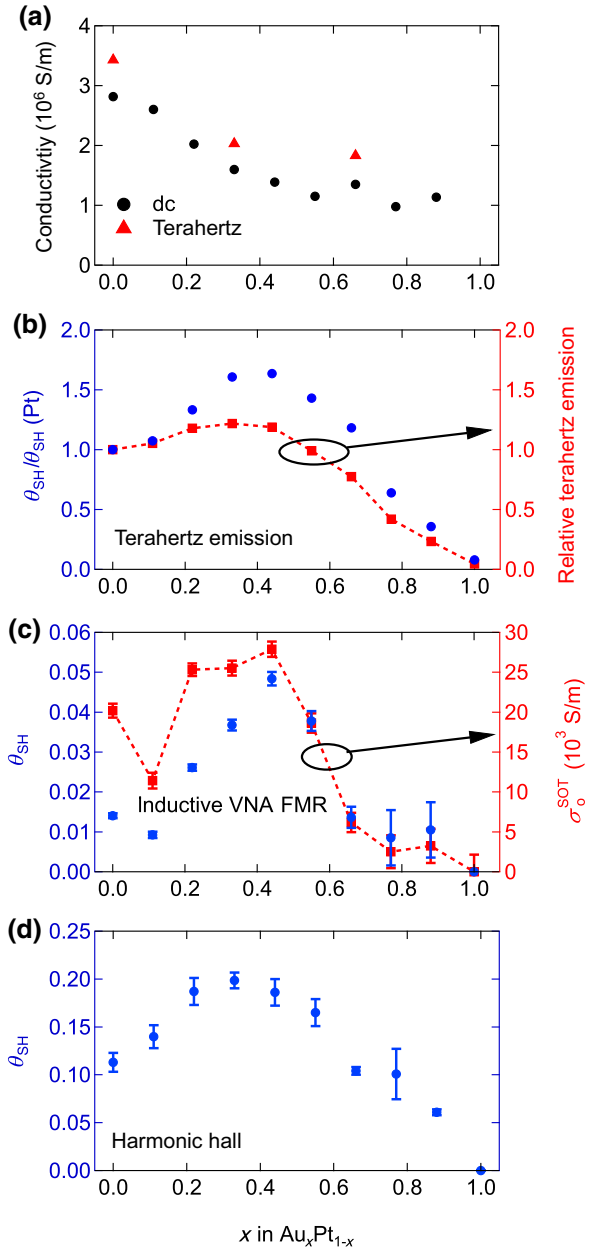

FIG. 2. (a) Electrical conductivities of the Au_xPt_{1-x} alloy films determined by four-point dc-conductivity measurements and by terahertz transmission measurements. In both cases, a parallel-conductor model is applied to subtract the conductance of the $Co_{40}Fe_{40}B_{20}$ layer. (b) Relative terahertz emission (right axis) and relative spin Hall angle (left axis) as obtained from Eq. (1). (c) Odd component of the spin-orbit-torque conductivity (right axis) obtained in the VNA-FMR measurements and extracted lower-bound spin Hall angle $\theta_{SH} = \sigma_o^{SOT}/\sigma_{xx}$ (left axis). (d) Spin Hall angles as determined with the harmonic-Hall-response method via Eq. (6).

B. Terahertz emission spectroscopy

In TES, a HM/FM bilayer is excited by a femtosecond laser pulse [Fig. 1(a)], thereby inducing ultrafast spin transport from the FM layer into the HM layer through an ultrafast version of the spin-dependent Seebeck effect [41–44]. In the HM, the laser-driven longitudinal spin current is converted into a transverse charge current by the inverse SHE. The resulting subpicosecond charge current

[45] gives rise to the emission of electromagnetic radiation at terahertz frequencies [41].

The terahertz waveforms in Fig. 1(d) are raw data obtained with this technique. The emission amplitudes are modeled as a function of terahertz frequency $\omega/2\pi$ as [41]

$$S_{\mathrm{THz}}(\omega) = AB(\omega)\lambda_s \tanh\left(\frac{t_{\mathrm{HM}}}{2\lambda_s}\right)\theta_{\mathrm{SH}} Z(\omega), \qquad (1)$$

where A is the pump-light absorptance, while the factor B captures the photon-to-spin-current conversion efficiency and the detector response function [46]. B is assumed to be independent of the alloy composition in our experiment, thereby ignoring possible variations of the spin-current strength due to, for example, variations of the interface quality for different Au concentrations.

The spatial shape of the spin current in the HM layer is captured by the spin-current relaxation length λ_s and the HM-layer thickness t_{HM}. According to transport theory based on the Boltzmann equation [47], λ_s equals the spin diffusion length at zero frequency, but becomes comparable to the mean free path at terahertz frequencies.

While the spin-to-charge-current conversion in Eq. (1) is quantified by θ_{SH}, the charge-current-to-electric-field conversion is described by the bilayer impedance

$$Z(\omega) = \frac{Z_0}{n_1(\omega) + n_2(\omega) + Z_0 \int_0^d dz \sigma_{xx}(z,\omega)}, \qquad (2)$$

where $n_1(\omega)$ and $n_2(\omega)$ are the refractive indices of air and the substrate, respectively, $Z_0 = 377\ \Omega$, and $\sigma_{xx}(z,\omega)$ is the in-plane conductivity of the material at depth z. For simplicity, we take σ_{xx} as constant across the film thickness and ignore the frequency dependence, because the frequencies used here are well below the Drude frequency of the material.

The SHA relative to a reference sample can be obtained for all alloy stoichiometries when λ_s is known. Here we take λ_s as the electron mean free path λ_{MF} and use $\lambda_{\mathrm{MF}}/\sigma_{zz} = 0.3 \times 10^{-15}\ \Omega\ \mathrm{m}^2$, where σ_{zz} is the electrical conductivity of the HM perpendicular to the film plane [6,40]. Measuring σ_{zz} is impractical, so we use the approximation $\sigma_{zz} \approx \sigma_{xx}$.

Note that θ_{SH} in Eq. (1) is an effective SHA, which, in addition to spin-to-charge-current conversion in the HM layer, contains such conversion also in the FM layer and at the FM/HM interface. Notably, all terahertz measurements (i.e., terahertz emission, pump absorptance, and terahertz conductivity) are conducted within less than 8 h.

C. VNA ferromagnetic resonance

In VNA FMR, we inductively detect microwave currents generated in HM/FM bilayers under the condition of FMR, which allows one to determine the SHC. The sample is placed face-down on a coplanar waveguide (CPW) [Fig. 1(b)]. A gigahertz current excites resonant spin precession (FMR) in the FM part of the bilayer. Because of spin pumping, a spin current flows into the HM layer, where it is converted into a charge current by the inverse SHE. The magnetic field created by this current couples back into the CPW and is extracted from the CPW transmission signal to obtain the complex-valued SOT conductivity σ^{SOT}. This quantity is directly linked to the SHC [48,49]. This technique is sensitive to the spin currents generated by the dynamic components of the magnetization only, which are in the film plane for the out-of-plane magnetic field configuration used here.

The raw data obtained by VNA FMR are the real and imaginary parts of the CPW transmission S_{21} as a function of the external magnetic field at fixed continuous-wave frequency [Fig. 1(e)]. The S_{21} data are fitted to Eq. (A1), and from Eq. (A3), we obtain the complex-valued normalized inductance $\widetilde{L}$ of the HM/FM bilayer at frequency ω. For each sample, the S_{21} measurements and extraction of $\widetilde{L}$ are performed for frequencies $5\ \mathrm{GHz} < \omega/2\pi < 40\ \mathrm{GHz}$. The generation of charge currents in the HM/FM bilayer under FMR conditions results in a linear frequency dependence of $\widetilde{L}$. The dc value $\widetilde{L}(\omega = 0)$ is the real-valued inductance of the HM/FM bilayer in the absence of any currents in the bilayer. To extract the complex-valued SOT conductivity $\sigma^{\mathrm{SOT}} = \sigma_e^{\mathrm{SOT}} + \mathrm{i}\sigma_o^{\mathrm{SOT}}$, $\widetilde{L}$ is fitted by [48]

$$\widetilde{L}\exp(i\phi_a) = \eta^2 \frac{\mu_0 t_{\mathrm{FM}} l}{4 w_C} + \eta\omega \frac{\hbar L_{12} \sigma^{\mathrm{SOT}}}{2eM_s}. \qquad (3)$$

The first term on the right side of Eq. (3) is the frequency-independent dipolar inductance stemming from the precessing magnetization. The second term is the linearly-frequency-dependent inductance due to the alternating currents flowing in the normal metal [48]. In Eq. (3), $w_C = 56\ \mu\mathrm{m}$ is the width of the CPW center conductor, $l = 8.7$ mm is the sample length, $L_{12}(d)$ is the mutual inductance between the sample and the CPW, and $0 < \eta(d) < 1$ is a unitless spacing loss as defined in Ref. [48]. The fit parameters are the separation d between the sample and the CPW, the anomalous phase ϕ_a, and the spin-orbit-torque conductivities σ_e^{SOT} and σ_o^{SOT}, where the even component σ_e^{SOT} also contains the effect of currents induced by Faraday's law of induction. The odd component σ_o^{SOT} is directly related to the dampinglike spin-orbit torque.

While the SOT conductivities can thus be directly measured by VNA FMR, extraction of the microscopic parameters, in particular the spin Hall angle, requires use of a suitable model and parameters [48,49]. A lower limit of the spin Hall angle can be obtained by

$$\theta_{\mathrm{SH}} = \sigma_o^{\mathrm{SOT}}/\sigma_{xx}, \qquad (4)$$

where we again assume $\sigma_{xx} \approx \sigma_{zz}$. Equation (4) assumes a completely transparent interface and thus vanishing spin

backflow and spin-memory loss (SML). As previously demonstrated [48,49], we thus may underestimate the spin Hall angle by a factor of approximately 10. This underestimation is predominantly caused by the expected strong SML in HM/FM bilayers [48,49]. Quantification of the SML is, in principle, possible but would require a thickness series of both HM and FM layers for each composition [49]. We use Eq. (4) here for a fair comparison of the VNA-FMR evaluation with the reference measurements based on the harmonic Hall response (see the next section), where the same assumptions are made.

D. Harmonic Hall response

Harmonic Hall voltage measurements are performed by injecting an alternating current with amplitude I_0 at frequency $\omega/2\pi$ into the Hall crosses measuring the in-phase first harmonic and out-of-phase second harmonic Hall voltages simultaneously on in-plane field rotation with a lock-in amplifier [Fig. 1(c)]. The SOT gives rise to a periodic deflection of the magnetization with in-plane and out-of-plane components, which can be detected via the planar Hall effect and the anomalous Hall effect, respectively. The second-harmonic out-of-phase Hall voltage rms value $V_{2\omega}$ depends on the in-plane angle φ between the current and the magnetization [Fig. 1(f)], and can be written as [34,39]

$$V_{2\omega} = \left(-\frac{B_{\mathrm{FL}}}{B_{\mathrm{ext}}} R_P \cos 2\varphi - \frac{1}{2}\frac{B_{\mathrm{DL}}}{B_{\mathrm{eff}}} R_A + \alpha' I_0\right) I_{\mathrm{rms}} \cos\varphi, \tag{5}$$

where $B_{\mathrm{eff}} = B_{\mathrm{ext}} + B_{\mathrm{sat}}$ is the effective field, and B_{FL} and B_{DL} are the current-induced effective field amplitudes associated with the fieldlike and dampinglike spin-orbit torques, respectively [19]. It is assumed that in-plane anisotropy fields (e.g., uniaxial and biaxial) are small compared with the external magnetic field B_{ext} (0.2–1 T) and can be ignored. The term $\alpha' I_0$ describes a parasitic contribution arising from the anomalous Nernst effect (ANE) [38], where $I_{\mathrm{rms}} = I_0/\sqrt{2}$. R_P and R_A are the amplitudes of the planar and anomalous Hall resistances at saturation, respectively. B_{ext} is the external magnetic field and B_{sat} is the perpendicular saturation field.

Equation (5) is fitted to the experimental data, and dampinglike effective fields and ANE contributions are separated by their dependence on the external field. The spin Hall angle is obtained from the dampinglike effective field as

$$\theta_{\mathrm{SH}} = \frac{2e}{\hbar}\frac{B_{\mathrm{DL}} M_s t_{\mathrm{FM}}}{j_{\mathrm{HM0}}}, \tag{6}$$

where j_{HM0} is the current-density amplitude in the heavy-metal layer far from the Hall-voltage pickup lines. In this expression, effects of spin-memory loss, spin backflow or spin transparency of the interface are ignored. Therefore, the SHA obtained by this formula is a strict lower bound to the true SHA of the HM layer. A correction factor of 1.45 for the inhomogeneous current flow in the Hall crosses is applied to the spin Hall angle, as suggested by a recent study on the influence of the aspect ratio of the Hall cross on the determination of the effective field [50].

E. First-principles calculations

For the first-principles calculations, we use the Kubo-Bastin linear-response theory as implemented in the Munich spin-polarized relativistic Korringa-Kohn-Rostoker (SPR-KKR) package [51–53]. Starting from a density-functional-theory description of the electronic structure of the chemically disordered alloy, we perform linear-response calculations including phonon effects via the alloy-analogy model to obtain the full spin-resolved conductivity tensor. The method treats the intrinsic SHC and the extrinsic effects on the same footing via so-called vertex corrections. In the nonzero-temperature calculations, the contributions due to the vertex corrections are, however, very small compared with the intrinsic spin Hall conductivity.

The longitudinal charge conductivity determined by the SPR-KKR package refers to the bulk. Interface scattering is known to reduce the conductivity σ_{xx} of thin films, which can be estimated via the Mayadas-Shatzkes (MS) model [54]:

$$\frac{\sigma_{xx}}{\sigma_{xx0}} = \left[1 + \frac{3\lambda_{\mathrm{MF}}}{8t_{\mathrm{HM}}}\left(1 + \frac{p}{2}\right) + \frac{3\lambda_{\mathrm{MF}}}{2D_{\mathrm{HM}}}\left(\frac{r}{1-r}\right)\right]^{-1}, \tag{7}$$

where σ_{xx0} is the bulk conductivity from the SPR-KKR calculation, t_{HM} is the film thickness, and D_{HM} is the lateral grain size. For our material system, the electron mean free path λ_{MF} is calculated as $\lambda_{\mathrm{MF}}/\sigma_{xx} = 0.3 \times 10^{-15}\ \Omega\ \mathrm{m}^2$. A reasonable fit of the data is obtained with $D_{\mathrm{HM}} \approx 5$ nm and both the specularity parameter p and the grain-boundary reflectivity parameter r set to 0.5.

III. RESULTS AND DISCUSSION

Figures 2(b) and 2(c) show the major results obtained with the three methods used here. For TES, Fig. 2(b) displays the terahertz emission amplitude (right axis) and the SHA as extracted with use of Eq. (1) (left axis). Both quantities are normalized to those of the pure Pt layer ($x = 0$). The terahertz emission amplitude exhibits a maximum at a Au fraction of $x \approx 0.4$, which is even more pronounced in the relative SHA. The reason for this difference is the monotonic decay of the HM conductivity [Fig. 2(a)] and the electron mean free path leading to a decreasing spin-current relaxation length λ_s with increasing x.

For the VNA-FMR measurements, Fig. 2(c) shows the odd component of the SOT conductivity (right axis) and the SHA (left axis) as obtained through Eq. (4). The SOT

conductivity features a broad plateau around $x \approx 0.33$ and decays with increasing Au content. $\sigma_o^{\mathrm{SOT}} \approx 2 \times 10^4$ S/m measured for $x = 0$ (pure Pt) is in good agreement with $\sigma_o^{\mathrm{SOT}} \approx 3 \times 10^4$ S/m measured for Pt/Ni-Fe with the same technique [48]. As the charge conductivity decreases with increasing x [Fig. 2(a)], a local maximum of θ_{SH} arises around $x \approx 0.4$.

Finally, the SHA as determined by the HHR method is displayed in Fig. 2(d). These measurements feature a local maximum around $x \approx 0.33$. As we determine both the SHA θ_{SH} and the conductivity σ_{xx} of the HM layer, we can also compute its SHC through $\sigma_{\mathrm{SH}} = \theta_{\mathrm{SH}}\sigma_{xx}$.

To better compare the results obtained with the three methods, Figs. 3(a) and 3(b) display, respectively, the measured SHAs and SHCs scaled to the HHR results for the pure Pt film ($x = 0$). We find that the scaled SHAs versus the Au fraction x show similar trends, in particular in terms of the position of the SHA maximum. All three results are also in reasonable agreement with a previous experiment on the Au-Pt system [17].

In particular, the TES data are in excellent overall agreement with the HHR data, with some discrepancies in both the SHA and the SHC around $x \approx 0.2$: the HHR method finds an initial increase of the SHC with increasing x, whereas the TES data suggest a monotonic decrease of the SHC with increasing x.

While TES delivers SHAs and SHCs relative to a reference HM (such as Pt), both VNA FMR and HHR provide absolute values. The HHR SHA of the 3-nm pure-Pt film ($x = 0$) is found to be approximately 0.11 ± 0.01, whereas the maximum SHA at $x = 0.33$ amounts to 0.20 ± 0.01. The $x = 0$ value of the SHA agrees very well with other recent measurements on Pt films with similar conductivities [6,10,31]. Our VNA-FMR SHA values of pure Pt are a factor of approximately 4–10 smaller than those from the HHR measurements. Because we assume vanishing spin backflow and vanishing SML for evaluation of both VNA-FMR and HHR data [see Eqs. (4) and (6)], this discrepancy indicates that at least one of these ignored parameters is substantially different between these techniques.

Because spin backflow is typically only a small correction for the investigated all-metallic FM/Pt system with effective spin-mixing conductances exceeding 10^{19} m^{-2} for metallic magnets [55], we speculate that the discrepancy is predominantly caused by a difference in SML.

SML [56] was found to be strong in previous FMR-based experiments [48,49,57,58], where up to 90% of the spin information can be lost at the metallic FM/Pt interface [48]. To reconcile our FMR and HHR measurements quantitatively in the context of SML alone, we have to assume a factor of 5–10 difference in SML between these two techniques. Unfortunately, the SML cannot be unambiguously determined from the existing sample series. We can thus only speculate that the difference might be due to one of the following reasons: (i) the VNA-FMR measurements are performed in an out-of-plane geometry and the HHR measurements are performed in an in-plane geometry; (ii) the VNA-FMR measurements are sensitive to the transverse dynamic magnetization components, while the HHR measurements are quasistatic. This could lead to enhanced spin dephasing in the FMR measurements, for instance in a thin layer of proximity-polarized Pt.

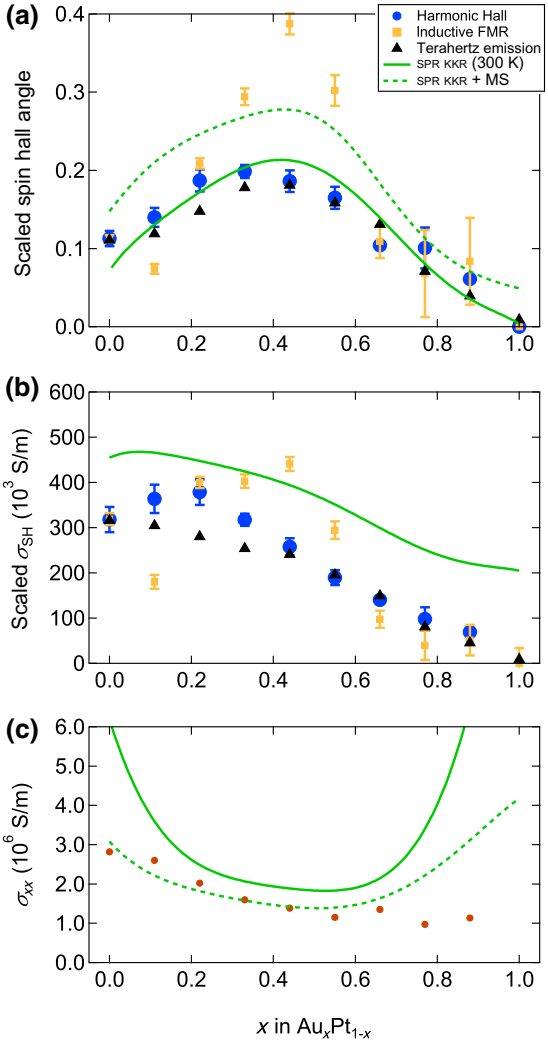

FIG. 3. (a) Experimental spin Hall angles scaled to the spin Hall angle of the pure-Pt sample obtained with the harmonic-Hall-response method. Green lines represent results from SPR-KKR calculations including or ignoring thin-film corrections of the conductivity via the MS model. (b) Scaled spin Hall conductivities as in (a). The green line represents the SPR-KKR calculation. (c) Electrical conductivity as measured electrically (dots), as calculated (green line), and as calculated including corrections from the MS model (dashed line).

Because no absolute values for the SHA can be extracted from the TES measurements, no conclusion about a possible SML at terahertz frequencies can be drawn. A quantitative evaluation of SML between the different experimental

geometries would be highly interesting but is left for future studies that concentrate on a single material system.

In addition to this possible dependence of the SML on the experimental geometry, further magnetization-direction-dependent corrections to the SHA may exist. For instance, a potential spin rotation at the interface [59] might depend on the geometry. All these corrections can, in addition, depend on the stoichiometry due to modifications of the film resistivities and the matching of the interfacial electronic structure.

To gain more insight into the observed composition dependence of the measured SHA, Fig. 3 also displays the unscaled first-principles results for the SHA, SHC, and charge conductivity of Au_xPt_{1-x} versus x. The experimental results for the SHA from the HHR method agree very well with the SPR-KKR calculation without the conductivity reduction from the MS model (see above). Inclusion of the MS model predicts a larger SHA for all stoichiometries. This effect can be traced back to the SHC, which is larger in the calculation than in the experiment [Fig. 3(b)]. At the same time, the film conductivity is smaller than what is predicted by SPR-KKR including the MS model for large Au content. The large deviation at high Au content can be attributed to island growth (see above), leading to strong grain-boundary scattering and thus to much lower conductivity than expected from the MS model with a single set of parameters.

Both techniques that provide quantitative results for the SHA and the SHC, the VNA-FMR method and the harmonic-Hall-response method, show smaller SHC than predicted by the SPR-KKR calculations. This trend may be explained by the already-mentioned ignoring of interfacial spin-memory loss. Other effects that may reduce the spin current include interfacial spin transparency and interfacial spin-orbit coupling [60]. The reduced spin-current density manifests itself either as less dampinglike spin-orbit torque observed in the harmonic Hall measurements or as less detected charge-current density in the inductive VNA-FMR experiment.

IV. CONCLUSION

Although an accurate determination of the internal SHA of a given material is of great fundamental interest, in high-throughput experiments it is often sufficient to observe a trend in relative terms rather than measure absolute values. To date, studies on the SHE have focused mostly on elements and binary alloys and compounds. Therefore, we are only at the beginning of mapping out the SHE in ternary, quaternary, and more-complex alloys and compounds. For an efficient search for materials with a large SHA or large SHC, high-throughput techniques for measuring these properties are necessary, and the two techniques presented here, VNA FMR and terahertz emission spectroscopy, are now proven tools for future experimental work.

ACKNOWLEDGMENTS

This work was supported by the German Research Foundation (DFG) through project WE5386/4-1, through TRR227 "Ultrafast spin dynamics" (projects B02 and A05), and by the European Research Council through ERC CoG TERAMAG (Grant No. 681917). We thank Günter Reiss for making available laboratory equipment.

APPENDIX

1. Sample fabrication

Thin-film heterostructures of the substrate Au_xPt_{1-x}(3 nm)/$Co_{40}Fe_{40}B_{20}$(3 nm)/Si(1.5 nm) are grown by magnetron sputtering at room temperature. For the terahertz emission experiments and for the inductive gigahertz measurements, we use polished fused-silica substrates. Si wafers with a 50-nm thermal oxide layer are used for the low-frequency harmonic Hall measurements. The Pt-Au alloys are made by magnetron co-sputtering from two elemental targets. All samples are exposed to a pure-oxygen plasma via the Si source before deposition to clean the substrate surface. The Pt-Au stoichiometries are verified by x-ray-fluorescence spectroscopy. For all samples, the film thicknesses and crystallographic phases are checked by x-ray-reflectivity and x-ray-diffraction measurements.

For the terahertz emission spectroscopy and the inductive gigahertz measurements, the samples are not subjected to further processing. For the harmonic Hall measurements, the samples on Si/SiO_x wafers are lithographically patterned into Hall crosses with an arm width of 16 μm and bonded into DIL-24 packages. During the lithographic processing, the films are heated to 90 °C for 20 min. No effect of the heating is seen in subsequent conductivity and x-ray-diffraction measurements.

2. Terahertz emission spectroscopy

The terahertz emission is driven with ultrashort laser pulses from a Ti:sapphire oscillator with a pulse duration of 10 fs, a central wavelength of 800 nm, a repetition rate of 80 MHz, and a pulse energy of about 1 nJ. The terahertz transient is measured via electro-optic sampling [61] in a 1-mm-thick ZnTe(110) crystal with a weak copropagating 10-fs near-infrared probe pulse from the same laser. The electrical conductivities of the Au-Pt alloy are obtained by terahertz transmission measurements as detailed in Refs. [44,62].

3. VNA-FMR measurements

A static magnetic field H is applied along the bilayer normal. FMR is excited by our passing a microwave current of fixed frequency ω through the CPW while sweeping

the magnitude of H. At each value of H, the complex-valued microwave transmission $S_{21}(H)$ through the CPW is recorded with the VNA. Experiments are repeated for 10 GHz $\leq \omega/2\pi \leq$ 40 GHz. For each ω, the $S_{21}(H)$ spectra obtained are fitted to

$$S_{21}(H) = S_{21}^{0} - iA\frac{\chi(H)}{M_s}, \tag{A1}$$

where S_{21}^{0} is the H-independent transmission through the CPW outside FMR conditions, A is a complex-valued scaling parameter, $\mu_0 M_s = 1.05$ T is the saturation magnetization, and

$$\chi(H) = \frac{M_s\,(H - M_{\text{eff}})}{(H - M_{\text{eff}} + i\Delta H)^2 - H_{\text{eff}}^2} \tag{A2}$$

is the diagonal component of the Polder susceptibility tensor [63]. Here $M_{\text{eff}} = H_{\text{res}} - H_{\text{eff}}$ and $H_{\text{eff}} = \omega/(\mu_0\gamma)$, where γ is the gyromagnetic ratio [64]. After fitting the data to Eq. (A1), as detailed in Ref. [64] we extract the normalized inductance [48]

$$\widetilde{L} = \frac{L}{\chi(H_{\text{res}})} = \frac{2AZ_0}{\omega M_s S_{21}^{0}}, \tag{A3}$$

with the impedance of the CPW $Z_0 = 50\ \Omega$. Because of the normalization by S_{21}^{0} in Eq. (A3), $\widetilde{L}$ is quantitatively determined without any calibration of the microwave circuit. Furthermore, the Gilbert damping α_{tot} is obtained by our fitting the ΔH-versus-ω data to

$$\Delta H = \frac{\omega}{\mu_0\gamma}\alpha_{\text{tot}} + \Delta H_0, \tag{A4}$$

with the inhomogeneous linewidth broadening ΔH_0. The VNA-FMR measurement technique is based on the principle of reciprocity [65] for excitation of magnetization dynamics and detection sensitivity and thus is independent of the exact driving field distribution in the sample as detailed in Refs. [48,66]. Possible microwave-magnetic-field shielding effects in the metallic films [67] are assumed to be negligible for our metallic thin film thickness of only 6 nm.

4. Harmonic Hall measurements

For determination of the spin Hall angle, the films are patterned into fourfold rotationally symmetric Hall crosses with conductor width $w = 16\ \mu$m and length $l = 48\ \mu$m by optical lithography. Harmonic-Hall-voltage measurements are performed in a dual Halbach cylinder array with a rotating magnetic field up to 1.0 T (MultiMag, Magnetic Solutions Ltd.). An alternating-current density with an rms value of $j_{\text{rms}} = 2 \times 10^{10}$A m^{-2} ($I_{\text{rms}} = 1.92$ mA) and frequency $\omega/2\pi = 3219$ Hz is injected into the Hall crosses, and the in-phase first harmonic and out-of-phase second harmonic Hall voltages are recorded simultaneously on in-plane field rotation with a Zurich Instruments MFLI multi-demodulator lock-in amplifier. The out-of-plane saturation component of the effective field $B_{\text{eff}} = B_{\text{ext}} + B_{\text{sat}}$ is $B_{\text{sat}} = B_{\text{dem}} - B_{\text{ani}} > 0$. It is obtained together with the anomalous-Hall-resistance amplitude R_A from Hall-voltage measurements in a perpendicular magnetic field up to 2.2 T. The planar Hall amplitudes R_P are obtained from the first-harmonic $V_\omega = R_P I_{\text{rms}} \sin 2\varphi$. The parasitic ANE component $\alpha' I_0$ yields an electric field $\mathbf{E}_{\text{ANE}} = -\alpha\nabla T \times \mathbf{m} \propto I_0^2$, where I_0 is the current amplitude. The prefactor α' summarizes all geometrical parameters and the film electrical conductivity, heat conductivity, etc., that determine ∇T. The magnetization of the $Co_{40}Fe_{40}B_{20}$ film is determined by alternating-gradient magnetometry to be $M_s = (1050 \pm 50)$ kA/m. The parallel-circuit model is applied to determine the current density flowing in the HM layer.

5. Linear-response calculations

The spin Hall conductivities are calculated within a fully relativistic multiple-scattering Green-function framework with use of the Kubo-Bastin formalism [14]. Intrinsic and extrinsic contributions to the spin Hall conductivity are treated on an equal footing. Furthermore, chemical alloying as well as the temperature are treated on an equal footing within the coherent potential approximation or the alloy-analogy model, respectively [51]. The formalism is implemented in the Munich SPR-KKR code [52,53]. The Green function is expanded up to $\ell_{\text{max}} = 3$ and the Fermi level is accurately obtained with Lloyd's formula. The atomic sphere approximation is used throughout. Dense k-point meshes are used to ensure accurate evaluation of the Brillouin-zone integrals for the Fermi surface term. For more details, see Ref. [17].

[1] M. I. Dyakonov and V. I. Perel, Current-induced spin orientation of electrons in semiconductors, Phys. Lett. A **35**, 459 (1971).

[2] J. E. Hirsch, Spin Hall Effect, Phys. Rev. Lett. **83**, 1834 (1999).

[3] A. Hoffmann, Spin hall effects in metals, IEEE Trans. Magn. **49**, 5172 (2013).

[4] J. Sinova, S. O. Valenzuela, J. Wunderlich, C. H. Back, and T. Jungwirth, Spin hall effects, Rev. Mod. Phys. **87**, 1213 (2015).

[5] T. Tanaka, H. Kontani, M. Naito, T. Naito, D. S. Hirashima, K. Yamada, and J. Inoue, Intrinsic spin hall effect and orbital hall effect in 4D and 5D transition metals, Phys. Rev. B **77**, 165117 (2008).

[6] E. Sagasta, Y. Omori, M. Isasa, M. Gradhand, L. E. Hueso, Y. Niimi, Y. C. Otani, and F. Casanova, Tuning the spin hall effect of Pt from the moderately dirty to the superclean regime, Phys. Rev. B **94**, 060412(R) (2016).

[7] C.-F. F. Pai, L. Liu, Y. Li, H. W. Tseng, D. C. Ralph, and R. A. Buhrman, Spin transfer torque devices utilizing the giant spin hall effect of tungsten, Appl. Phys. Lett. **101**, 122404 (2012).

[8] L. Liu, C.-F. Pai, Y. Li, H. W. Tseng, D. C. Ralph, and R. A. Buhrman, spin-torque switching with the giant Spin hall effect of Tantalum, Science (80) **336**, 555 (2012).

[9] X. Qiu, P. Deorani, K. Narayanapillai, K.-S. Lee, K.-J. Lee, H.-W. Lee, and H. Yang, Angular and temperature dependence of current induced spin-orbit effective fields in Ta/CoFeB/MgO nanowires, Sci. Rep. **4**, 4491 (2014).

[10] M.-H. Nguyen, D. C. Ralph, and R. A. Buhrman, Spin Torque Study of the Spin Hall Conductivity and Spin Diffusion Length in Platinum Thin Films with Varying Resistivity, Phys. Rev. Lett. **116**, 126601 (2016).

[11] T. Schulz, K. Lee, B. Krüger, R. Lo Conte, G. V. Karnad, K. Garcia, L. Vila, B. Ocker, D. Ravelosona, and M. Kläui, Effective field analysis using the full angular spin-orbit torque magnetometry dependence, Phys. Rev. B **95**, 224409 (2017).

[12] W. Zhang, W. Han, X. Jiang, S.-H. Yang, and S. S. P. Parkin, Role of transparency of platinum–ferromagnet interfaces in determining the intrinsic magnitude of the spin hall effect, Nat. Phys. **11**, 496 (2015).

[13] F. Freimuth, S. Blügel, and Y. Mokrousov, Anisotropic Spin Hall Effect from First Principles, Phys. Rev. Lett. **105**, 246602 (2010).

[14] S. Lowitzer, M. Gradhand, D. Ködderitzsch, D. V. Fedorov, I. Mertig, and H. Ebert, Extrinsic and Intrinsic Contributions to the Spin Hall Effect of Alloys, Phys. Rev. Lett. **106**, 056601 (2011).

[15] M. Gradhand, D. V Fedorov, F. Pientka, P. Zahn, I. Mertig, and B. L. Györffy, First-principle calculations of the berry curvature of bloch states for charge and spin transport of electrons, J. Phys. Condens. Matter **24**, 213202 (2012).

[16] D. Ködderitzsch, K. Chadova, and H. Ebert, Linear response kubo-bastin formalism with application to the anomalous and spin hall effects: A first-principles approach, Phys. Rev. B **92**, 184415 (2015).

[17] M. Obstbaum, M. Decker, A. K. Greitner, M. Haertinger, T. N. G. Meier, M. Kronseder, K. Chadova, S. Wimmer, D. Ködderitzsch, H. Ebert, and C. H. Back, Tuning Spin Hall Angles by Alloying, Phys. Rev. Lett. **117**, 167204 (2016).

[18] A. Manchon and S. Zhang, Theory of spin torque due to spin-orbit coupling, Phys. Rev. B **79**, 094422 (2009).

[19] K. Garello, I. M. Miron, C. O. Avci, F. Freimuth, Y. Mokrousov, S. Blügel, S. Auffret, O. Boulle, G. Gaudin, and P. Gambardella, Symmetry and magnitude of spin-orbit torques in ferromagnetic heterostructures, Nat. Nanotechnol. **8**, 587 (2013).

[20] L. Liu, C.-F. Pai, D. C. Ralph, and R. A. Buhrman, Magnetic Oscillations Driven by the Spin Hall Effect in 3-Terminal Magnetic Tunnel Junction Devices, Phys. Rev. Lett. **109**, 186602 (2012).

[21] I. Mihai Miron, G. Gaudin, S. Auffret, B. Rodmacq, A. Schuhl, S. Pizzini, J. Vogel, and P. Gambardella, Current-driven spin torque induced by the Rashba effect in a ferromagnetic metal layer, Nat. Mater. **9**, 230 (2010).

[22] I. M. Miron, K. Garello, G. Gaudin, P.-J. Zermatten, M. V. Costache, S. Auffret, S. Bandiera, B. Rodmacq, A. Schuhl, and P. Gambardella, Perpendicular switching of a single ferromagnetic layer induced by in-plane current injection, Nature **476**, 189 (2011).

[23] M. Cubukcu, O. Boulle, M. Drouard, K. Garello, C. Onur Avci, I. Mihai Miron, J. Langer, B. Ocker, P. Gambardella, and G. Gaudin, Spin-orbit torque magnetization switching of a three-terminal perpendicular magnetic tunnel junction, Appl. Phys. Lett. **104**, 42406 (2014).

[24] K. Garello, C. O. Avci, I. M. Miron, M. Baumgartner, A. Ghosh, S. Auffret, O. Boulle, G. Gaudin, and P. Gambardella, Ultrafast magnetization switching by spin-orbit torques, Appl. Phys. Lett. **105**, 212402 (2014).

[25] S. Fukami, C. Zhang, S. DuttaGupta, A. Kurenkov, and H. Ohno, Magnetization switching by spin–orbit torque in an antiferromagnet–ferromagnet bilayer system, Nat. Mater. **15**, 535 (2016).

[26] Y.-C. Lau, D. Betto, K. Rode, J. M. D. Coey, and P. Stamenov, Spin–orbit torque switching without an external field using interlayer exchange coupling, Nat. Nanotechnol. **11**, 758 (2016).

[27] M. Weiler, J. M. Shaw, H. T. Nembach, and T. J. Silva, Phase-Sensitive Detection of Spin Pumping via the ac Inverse Spin Hall Effect, Phys. Rev. Lett. **113**, 157204 (2014).

[28] L. Liu, T. Moriyama, D. C. Ralph, and R. A. Buhrman, Spin-Torque Ferromagnetic Resonance Induced by the Spin Hall Effect, Phys. Rev. Lett. **106**, 036601 (2011).

[29] T. Kimura, Y. Otani, T. Sato, S. Takahashi, and S. Maekawa, Room-Temperature Reversible Spin Hall Effect, Phys. Rev. Lett. **98**, 156601 (2007).

[30] H. Nakayama, M. Althammer, Y.-T. Chen, K. Uchida, Y. Kajiwara, D. Kikuchi, T. Ohtani, S. Geprägs, M. Opel, S. Takahashi, R. Gross, G. E. W. Bauer, S. T. B. Goennenwein, and E. Saitoh, Spin Hall Magnetoresistance Induced by a Nonequilibrium Proximity Effect, Phys. Rev. Lett. **110**, 206601 (2013).

[31] C.-F. Pai, M. Mann, A. J. Tan, and G. S. D. Beach, Determination of spin torque efficiencies in heterostructures with perpendicular magnetic anisotropy, Phys. Rev. B **93**, 144409 (2016).

[32] D. Qu, S. Y. Huang, G. Y. Guo, and C. L. Chien, Inverse spin hall effect in $Au_xTa_1 - x$ alloy films, Phys. Rev. B **97**, 024402 (2018).

[33] E. Derunova, Y. Sun, C. Felser, S. S. P. Parkin, B. Yan, and M. N. Ali, Giant intrinsic spin hall effect in W_3Ta and other A15 superconductors, Sci. Adv. **5**, eaav8575 (2019).

[34] K. Fritz, S. Wimmer, H. Ebert, and M. Meinert, Large spin hall effect in an amorphous binary alloy, Phys. Rev. B **98**, 094433 (2018).

[35] J. Cramer, T. Seifert, A. Kronenberg, F. Fuhrmann, G. Jakob, M. Jourdan, T. Kampfrath, and M. Kläui, Complex terahertz and direct current inverse spin hall effect in $YIG/Cu_1 - xIr_x$ bilayers across a wide concentration range, Nano Lett. **18**, 1064 (2018).

[36] U. H. Pi, K. Won Kim, J. Y. Bae, S. C. Lee, Y. J. Cho, K. S. Kim, and S. Seo, Tilting of the spin orientation induced by Rashba effect in ferromagnetic metal layer, Appl. Phys. Lett. **97**, 162507 (2010).

[37] M. Hayashi, J. Kim, M. Yamanouchi, and H. Ohno, Quantitative characterization of the spin-orbit torque using

harmonic hall voltage measurements, Phys. Rev. B **89**, 144425 (2014).

[38] C. O. Avci, K. Garello, M. Gabureac, A. Ghosh, A. Fuhrer, S. F. Alvarado, and P. Gambardella, Interplay of spin-orbit torque and thermoelectric effects in ferromagnet/normal-metal bilayers, Phys. Rev. B **90**, 224427 (2014).

[39] Y. Wen, J. Wu, P. Li, Q. Zhang, Y. Zhao, A. Manchon, J. Q. Xiao, and X. Zhang, Temperature dependence of spin-orbit torques in Cu-Au alloys, Phys. Rev. B **95**, 104403 (2017).

[40] S. Dutta, K. Sankaran, K. Moors, G. Pourtois, S. Van Elshocht, J. Bömmels, W. Vandervorst, Z. TVkei, and C. Adelmann, Thickness dependence of the resistivity of platinum-group metal thin films, J. Appl. Phys. **122**, 025107 (2017).

[41] T. Seifert *et al.*, Efficient metallic spintronic emitters of ultrabroadband terahertz radiation, Nat. Photonics **10**, 483 (2016).

[42] A. Alekhin, I. Razdolski, N. Ilin, J. P. Meyburg, D. Diesing, V. Roddatis, I. Rungger, M. Stamenova, S. Sanvito, U. Bovensiepen, and A. Melnikov, Femtosecond Spin Current Pulses Generated by the Nonthermal Spin-Dependent Seebeck Effect and Interacting with Ferromagnets in Spin Valves, Phys. Rev. Lett. **119**, 017202 (2017).

[43] T. Kampfrath, M. Battiato, P. Maldonado, G. Eilers, J. Nötzold, S. Mährlein, V. Zbarsky, F. Freimuth, Y. Mokrousov, S. Blügel, M. Wolf, I. Radu, P. M. Oppeneer, and M. Münzenberg, Terahertz spin current pulses controlled by magnetic heterostructures, Nat. Nanotechnol. **8**, 256 (2013).

[44] T. Seifert *et al.*, Terahertz spin currents and inverse spin hall effect in thin-film heterostructures containing complex magnetic compounds, SPIN **7**, 1740010 (2017).

[45] T. S. Seifert *et al.*, Femtosecond formation dynamics of the spin seebeck effect revealed by terahertz spectroscopy, Nat. Commun. **9**, 2899 (2018).

[46] L. Braun, G. Mussler, A. Hruban, M. Konczykowski, T. Schumann, M. Wolf, M. Münzenberg, L. Perfetti, and T. Kampfrath, Ultrafast photocurrents at the surface of the three-dimensional topological insulator Bi_2Se_3, Nat. Commun. **7**, 13259 (2016).

[47] Y.-H. Zhu, B. Hillebrands, and H. C. Schneider, Signal propagation in time-dependent spin transport, Phys. Rev. B **78**, 054429 (2008).

[48] A. J. Berger, E. R. J. Edwards, H. T. Nembach, A. D. Karenowska, M. Weiler, and T. J. Silva, Inductive detection of fieldlike and dampinglike ac inverse spin-orbit torques in ferromagnet/normal-metal bilayers, Phys. Rev. B **97**, 094407 (2018).

[49] A. J. Berger, E. R. J. Edwards, H. T. Nembach, O. Karis, M. Weiler, and T. J. Silva, Determination of the spin hall effect and the spin diffusion length of Pt from self-consistent fitting of damping enhancement and inverse spin-orbit torque measurements, Phys. Rev. B **98**, 024402 (2018).

[50] L. Neumann and M. Meinert, Influence of the hall-bar geometry on harmonic hall voltage measurements of spin-orbit torques, AIP Adv. **8**, 095320 (2018).

[51] H. Ebert, S. Mankovsky, K. Chadova, S. Polesya, J. Minár, and D. Ködderitzsch, Calculating linear-response functions for finite temperatures on the basis of the alloy analogy model, Phys. Rev. B **91**, 165132 (2015).

[52] H. Ebert, D. Ködderitzsch, and J. Minár, Calculating condensed matter properties using the KKR-green's function method–recent developments and applications, Rep. Prog. Phys. **74**, 96501 (2011).

[53] H. Ebert *et al.*, The Munich SPR-KKR package, version 7.7, https://www.ebert.cup.uni-muenchen.de/ (2017).

[54] A. F. Mayadas and M. Shatzkes, Electrical-resistivity model for polycrystalline films: The case of arbitrary reflection at external surfaces, Phys. Rev. B **1**, 1382 (1970).

[55] F. D. Czeschka, L. Dreher, M. S. Brandt, M. Weiler, M. Althammer, I.-M. Imort, G. Reiss, A. Thomas, W. Schoch, W. Limmer, H. Huebl, R. Gross, and S. T. B. Goennenwein, Scaling Behavior of the Spin Pumping Effect in Ferromagnet-Platinum Bilayers, Phys. Rev. Lett. **107**, 046601 (2011).

[56] Y. Liu, Z. Yuan, R. J. H. Wesselink, A. A. Starikov, and P. J. Kelly, Interface Enhancement of Gilbert Damping from First Principles, Phys. Rev. Lett. **113**, 207202 (2014).

[57] J.-C. Rojas-Sánchez, N. Reyren, P. Laczkowski, W. Savero, J.-P. Attané, C. Deranlot, M. Jamet, J.-M. George, L. Vila, and H. Jaffrès, Spin Pumping and Inverse Spin Hall Effect in Platinum: The Essential Role of Spin-Memory Loss at Metallic Interfaces, Phys. Rev. Lett. **112**, 106602 (2014).

[58] M. W. Keller, K. S. Gerace, M. Arora, E. K. Delczeg-Czirjak, J. M. Shaw, and T. J. Silva, Near-unity spin hall ratio in $Ni_xCu_1 - x$ alloys, Phys. Rev. B **99**, 214411 (2019).

[59] A. M. Humphries, T. Wang, E. R. J. Edwards, S. R. Allen, J. M. Shaw, H. T. Nembach, J. Q. Xiao, T. J. Silva, and X. Fan, Observation of spin-orbit effects with spin rotation symmetry, Nat. Commun. **8**, 911 (2017).

[60] V. P. Amin and M. D. Stiles, Spin transport at interfaces with spin-orbit coupling: Formalism, Phys. Rev. B **94**, 104419 (2016).

[61] A. Leitenstorfer, S. Hunsche, J. Shah, M. C. Nuss, and W. H. Knox, Detectors and sources for ultrabroadband electro-optic sampling: Experiment and theory, Appl. Phys. Lett. **74**, 1516 (1999).

[62] T. Seifert, N. M. Tranh, O. Gueckstock, S. M. Rouzegar, L. Nadvornik, S. Jaiswal, G. Jakob, V. Temnov, M. Muenzenberg, M. Wolf, M. Kläui, and T. Kampfrath, Terahertz spectroscopy for all-optical spintronic characterization of the spin-hall-effect metals Pt, W and Cu_80Ir_20, J. Phys. D: Appl. Phys. **51**, 364003 (2018).

[63] L. Dreher, M. Weiler, M. Pernpeintner, H. Huebl, R. Gross, M. S. Brandt, and S. T. B. Goennenwein, Surface acoustic wave driven ferromagnetic resonance in nickel thin films: Theory and experiment, Phys. Rev. B **86**, 134415 (2012).

[64] H. T. Nembach, T. J. Silva, J. M. Shaw, M. L. Schneider, M. J. Carey, S. Maat, and J. R. Childress, Perpendicular ferromagnetic resonance measurements of damping and Landé g-factor in sputtered $(Co_2Mn)_1 - xGe_x$ thin films, Phys. Rev. B **84**, 054424 (2011).

[65] T. Wessel-Berg and H. Bertram, A generalized formula for induced magnetic flux in a playback head, IEEE Trans. Magn. **14**, 129 (1978).

[66] T. J. Silva, H. T. Nembach, J. M. Shaw, B. Doyle, K. Oguz, K. O'Brien, and M. Doczy, in Metrology and Diagnostic Techniques for Nanoelectronics, edited by Z. Ma and D. G. Seiler (Pan Stanford, Singapore, 2017), p. 849.

[67] Ivan S. Maksymov and M. Kostylev, Impact of conducting nonmagnetic layers on the magnetization dynamics in thin-film magnetic nanostructures, J. Appl. Phys. **113**, 043927 (2013).